This is a preprint, the final version is subject to change, of the American Mineralogist (MSA)
Cite as Authors (Year) Title. American Mineralogist, in press.
(DOI will not work until issue is live.) DOI: http://dx.doi.org/10.2138/am.2013.4420

Revision 1

On the effect of carbonate on barite growth at elevated temperatures

Nuria Sánchez-Pastor[1], Melanie Kaliwoda[2],

Sabino Veintemillas-Verdaguer[3] and Guntram Jordan[4]

[1]Departamento de Cristalografía y Mineralogía, Universidad Complutense de Madrid, 28040, Madrid, Spain

[2]Mineralogische Staatssammlung München, 80333 München, Germany

[3]Instituto de Ciencia de Materiales de Madrid CSIC, C/ Sor Juana Inés de la Cruz 3, Cantoblanco, 28049, Madrid, Spain

[4]Department für Geo- und Umweltwissenschaften, Ludwig-Maximilians-Universität, 80333 München, Germany

ABSTRACT

The effect of carbonate on the growth of barite {001} surfaces from aqueous solutions supersaturated with respect to barite ($\Omega_{barite} \sim 12$) was studied by hydrothermal atomic force microscopy (HAFM) and Raman spectroscopy at temperatures ranging from 25 °C to 70 °C. The experiments showed that the effects of carbonate depend on the specific location of growth. For mono-layers growing on pristine barite, the carbonate-additive promotes growth and the spreading rate of two-dimensional islands increases with temperature. However, growth is inhibited in layers growing on surfaces which grew in carbonate containing solution. The threshold carbonate concentration necessary to completely inhibit growth is inversely correlated with temperature. Raman spectroscopy revealed the presence of carbonate within crystals which grew in carbonate containing solution. Judging by these findings, incorporation of carbonate into the structure of growing barite as a thermally activated process likely is a controlling factor which inhibits barite growth. Thus the study shows that additives can exert opposing effects on growth not only depending on additive concentration but also depending on the specific growth location. The implication of this work, therefore, is that bimodal effects of additives on crystal growth occur more frequent than generally recognized. The insights into the mechanisms of such bimodal effects of additives can significantly contribute to the understanding and predictability of the kinetics of macro-scale processes such as barite scale formation or the behavior of barium sulfate in CO_2-sequestration fluids.

Keywords: Barite, Hydrothermal Atomic Force Microscopy, Impurity, Growth Inhibition, Growth Promotion, Carbonate, Raman Spectroscopy.

INTRODUCTION

Barite ($BaSO_4$) occurs in a wide variety of geologic environments from the early Archean to the present (Hanor 2000). Due to its low solubility in water ($K_{sp} = 10^{-9.96}$ at 20 ºC, Blount 1977), barite precipitation and dissolution control the geochemical distribution of barium in surface waters as well as in crustal fluids. Mixing of Ba-rich hydrothermal fluids with sulfate-rich meteoric or ocean fluids produces supersaturated solutions and results in a rapid precipitation (Hanor 1994). Crystal growth from solution is a complex process comprising of several steps from bulk diffusion to the final incorporation of the growth unit (Nielsen 1984; Sunawaga 1993; Astilleros et al. 2006). Impurities in the growth medium strongly influence the kinetics of growth (Sangwal 1993). Therefore, the effects of additives on crystal growth kinetics have been studied extensively (Davey 1976; Davey and Mullin, 1974a, 1974b; Kubota and Mullin 1995; Kubota 2001; Kubota et al. 1999; Rauls et al. 2000; Sangwal 1993; Sánchez-Pastor et al. 2007; Sunagawa 1987). High resolution AFM investigations and numerical methods have gained insights into the molecular processes leading to the observed effects (Astilleros et al. 2010; Bosbach et al. 1998; De Yoreo et al. 2001; Dove and Hochella 1993; Freij et al. 2004; Higgins et al. 2000; Kuwahara 2011; Pina et al. 1998; Reyhani et al. 2002; Risthaus et al. 2001; Stack et al. 2012). Because carbonate is one of the most important anions in meteoric waters, the effects of carbonate on the growth of barite are particularly relevant. Sánchez-Pastor et al. 2006 studied the effects of carbonate at room temperature and various levels of supersaturation. The study revealed that the step kinematics on both {001} and {210} faces were strongly affected by the presence of carbonate: While the advance of steps of the first growth layer was promoted, an increasing inhibition with increasing carbonate concentration was found for the steps in the second layer. Above a certain threshold concentration, step advance completely ceased i.e., a dead zone was

reached (c.f. Cabrera and Vermilyea 1958; Land et al. 1999; Sangwal and Owczarek 1993; van Enckevort et al. 1996).

The aim of this work was to study the effects of carbonate at elevated temperatures using Raman spectroscopy and hydrothermal atomic force microscopy (HAFM; c.f. Higgins et al. 1998a, 1998b, 2002; Jordan and Astilleros 2006; Jordan et al. 2007; Sanchez-Pastor et al. 2010) in order to obtain answers to the questions: i) How does the carbonate concentration affect the growth kinetics of the first and second monolayer above room temperature? ii) Does the presence of carbonate ions affect the morphology of the two dimensional islands? iii) What is the temperature dependence of the threshold carbonate concentration necessary to inhibit growth?

EXPERIMENTAL PROCEDURE

HAFM experiments

In-situ HAFM experiments were carried out on barite {001} surfaces. Optically clear and colourless natural barite crystals (León, Spain) were cleaved along (001) with a razor blade. Samples were mechanically mounted into the AFM fluid cell using a Ti-wire; no adhesives were used. A continuous flow (> 0.2 mL/min) of solution through the fluid cell (volume ≈ 0.5 mL) was established by a gravity feed. Temperatures ranged from 25 °C to 70 °C. Due to the temperature dependence of the barite solubility (Blount 1977), the concentrations of Ba^{2+} and SO_4^{2-} had to be adjusted for the chosen supersaturation $\Omega_{barite} \sim 12$ ($\Omega_{barite} = a(Ba^{2+})\cdot a(SO_4^{2-})/K_{sp,barite}$ where $a(Ba^{2+})$ and $a(SO_4^{2-})$ are the activities of the free ions in the solution and $K_{sp,barite}$ is the barite solubility product). The according activities were calculated using PHREEQC (Parkhurst and Appelo 1999). Table 1 summarises the concentrations of $BaCl_2$, Na_2SO_4 and Na_2CO_3 used at 25, 40, 50, 60 and 70 °C as well as

Ω_{barite} and $\Omega_{witherite}$. All solutions were strongly undersaturated with respect to witherite. The growth solutions were prepared from commercial reagent grade $BaCl_2$, Na_2SO_4 and Na_2CO_3 dissolved in high purity deionized water (resistivity: 18 MΩ.cm) which was equilibrated with the ambient atmosphere before adding further reagents. The pH of the carbonated solutions varied from 8 to 10 causing carbonate and bicarbonate to be the dominant species. Systematic measurements of the step advance rates were taken on the barite surface along the [100] direction of the two-dimensional islands (Fig. 1a). To ensure reproducibility, experiments were repeated 2 or 3 times on different barite samples.

Micro- Raman spectroscopy experiments

To further characterize the influence of temperature and the possible incorporation of carbonate into the structure, Raman spectroscopic analyses were performed. For this purpose, natural barite crystals were cleaved along the (001) surface and placed within a batch reactor (volume ~ 1000 mL). The reactor was filled with a solution supersaturated with respect to barite (Ω_{barite} = 12.3, $\Omega_{witherite}$ = 0.03) and containing 0.03 mM sodium carbonate at 50 ºC (carbonate speciation $a(CO_3^{2-})$ = $0.1x10^{-5}$ M, $a(HCO_3^-)$ = $2.8x10^{-5}$ M). For Raman measurements, the crystals were removed from the solution after 240 hours.

Raman spectra were taken with a confocal micro-Raman spectrometer (HORIBA; XploRa-Raman-System). For excitation we used the second harmonic generation (532 nm, P_{max} = 15 mW) of a Nd-YAG laser, focused with a 100x long-wide-distance objective (Olympus) and a beam diameter of 0.7 µm. The beam was transmitted through an optical fibre to the spectrometer using a 50 µm diameter fibre core as a pinhole for the confocal setup. The diffraction limited focus resulted in a lateral resolution of about 400 nm and a focal depth of about 800 nm. Due to the TEM00 laser mode, the power distribution within the laser beam

129 profile was Gaussian. Therefore, the energy input in the central region was higher than at the
130 rim of the laser spot. A sharp edge filter removed elastically scattered photons. For the
131 measurements a 100 % filter and a 1200 T grating was used. All spectra were analyzed using
132 FITYK curve fitting and data processing software (Wojdyr 2010).
133
134 **RESULTS AND DISCUSSION**
135
136 At 25 °C, two-dimensional islands (half unit cell in height) nucleated and spread on
137 the barite (001) surface (Fig. 1a). The islands were bound by two straight edges parallel to the
138 <120> directions and one curved edge. Due to the symmetry of the barite structure, with a
139 binary screw axis perpendicular to the surface, islands on consecutive (001) layers are rotated
140 by 180° (Fig. 1b; c.f. Hartman and Strom 1989; Pina et al. 1998; Sánchez-Pastor 2006). As a
141 reference, the spreading rate of the two-dimensional islands were measured along [100] in
142 pure solutions at different temperatures (Table 1). The spreading rates increased exponentially
143 with temperature. A rate of 0.54 ± 0.01 nm/s and 4.2 ± 0.3 nm/s was measured at 25 ºC and
144 70 ºC, respectively. The increase of the velocities with temperature fits very well to an
145 Arrhenius behavior (Fig. 2) yielding an apparent activation energy E_a of 38 ± 1 kJ/mol.
146 Higgins et al. (2000) reported an effective activation energy of approx. 44 kJ/mol from
147 measured velocities of <120> bilayer steps in the temperature range of 90 to 125 °C and
148 supersaturation $1< \Omega <1.7$.
149
150 In carbonate containing solutions ($\Omega_{barite} \sim 12$) at 25 °C, the islands growing directly
151 on pristine barite surface showed the characteristic circular sector shape with straight edges
152 parallel to the <120> directions. Furthermore, the spreading rates of islands growing directly
153 on the pristine barite surface increased with increasing carbonate concentration and

154 temperature (Table 2 and Sánchez-Pastor, 2006). Above 60 ºC, the rates were so high that
155 quantitative measurements were not possible any longer.
156
157 Figure 3 shows the evolution of the barite (001) surface during the exchange of a pure
158 solution for a carbonate containing solution (total carbonate *Tc* = 0.06 mM) at 50 °C. Four
159 two-dimensional islands can be seen (Fig. 3a) which had been formed in the carbonate-free
160 solution. 54 minutes later (Fig. 3b), a new generation of islands was formed on the surface.
161 After the acquisition of the data shown in Figure 3b, the solution in the cell was exchanged
162 for the carbonate containing solution. Thus, the islands grew in the presence of carbonate but
163 still on pristine barite surface on which they coalesced and formed a complete monolayer
164 (Fig. 3c). The initial stage of formation of the second monolayer can be observed in Figure
165 3d. The islands of the second monolayer (marked) started to grow on those areas that had
166 been grown in the absence of carbonate (e.g. on top of the islands marked in Fig. 3b).
167 However, the shape of the new islands differs from the shape of the islands on the first
168 monolayer. In Figure 3e, the beginning of the formation of the third monolayer can be seen.
169 Steps increasingly roughened and the island morphology turned elliptical (the latter only if
170 $a(CO_3) > 0.4 \times 10^{-5}$ M and T ≥40 °C). In Figure 3f (taken 145 minutes after Fig. 3a), steady
171 state growth was established by nucleation, spreading and coalescence of islands with rough
172 elliptical steps.
173
174 In Figure 4, the spreading rates of the islands along the [100] direction within the
175 second and higher layers have been plotted versus the activity of carbonate in the solution for
176 25 °C, 40 °C, and 50 °C. Table 2 shows the according activities of the carbonate and
177 bicarbonate species. The data at 25 °C (squares) were taken from Sánchez-Pastor et al.
178 (2006). At 25 °C, the spreading rate of second layer islands was 0.54 nm/s for $a(CO_3^{2-})$
179 activities $< 0.7 \times 10^{-5}$ M. For $a(CO_3^{2-}) > 6.6 \times 10^{-5}$ M, growth of second layer islands was

completely inhibited. Islands only grew either on pristine barite or on layers previously grown in the absence of carbonate. In the case of carbonated solutions at 40 °C (circles in Fig. 4), the growth rate of second layer islands remained constant at ~1.3 nm/s for $a(CO_3^{2-}) < 0.1 \times 10^{-5}$ M. For higher activities, the rate decreased as the concentration increased. The concentration required to completely inhibit growth at 40 °C was 1.4×10^{-5} M. At 50 °C, the rate in presence of low carbonated solutions (triangles in Fig. 4) is approx. three times higher than at 25 °C. Also at this temperature, the spreading rate decreased with increasing carbonate concentration. Moreover, $a(CO_3^{2-})$ required to completely inhibit growth was 0.62×10^{-5} M.

While the spreading rate of the first layer increases with increasing carbonate concentration, the findings for the second and higher layers can be summarized as follows: i) at low carbonate concentrations spreading rates of two-dimensional islands increase with increasing temperatures; ii) with increasing carbonate concentration spreading rates decrease; iii) this decrease of rates becomes more pronounced with increasing temperature; iv) the threshold carbonate concentrations to attain full inhibition decrease with increasing temperature. The increasing inhibitor-effect of carbonate with increasing temperature points to a thermally activated process. AFM observations revealed (Fig. 3) step roughening and changes of the shape of the two-dimensional islands in carbonate containing solutions. Therefore, the thermally activated inhibiting process is likely located at the surface of the barite crystals. At this location CO_3^{2-} chemisorption and/or incorporation can cause the observed inhibition. Chemisorption has been suggested to be the major inhibition process for instance for calcite growth in the presence of Sr (Bracco et al. 2012). The effect of carbonate on barite growth, however, can hardly be explained by chemisorption solely. Chemisorption likely takes place on all layers to a similar extent. A uniform effect on all layers should be the consequence rather than the observed layer dependent effect of carbonate.

Irrespective of the difference between the effects of carbonate on barite growth and Sr on calcite growth, the ratio of the solution activity of the additive and the constituent ion at which the spreading rate is one-half of the maximum rate can be calculated (i.e. [$a(CO_3^{2-})/a(SO_4^{2-})$] at $R_{max/2}$; see Bracco et al. 2012). However, the temperature dependent CO_3^{2-}/SO_4^{2-}-data obtained here allow further evaluation by plotting the logarithm of the CO_3^{2-}/SO_4^{2-}-ratios at half spreading rate vs. reciprocal absolute temperature (Fig. 5). The plot shows a linear relationship. Following the reasoning of Bracco et al. (2006), a free energy of carbonate incorporation of $\Delta G = -40\pm3$ kJ/mol can be derived from the slope of the linear relation. The similarity of this value and the apparent activation energy for step advancement (see above) supports the assumption of competitive incorporation of carbonate and sulfate.

In order to clarify whether the growing barite crystal incorporates significant amounts of carbonate, micro-Raman spectroscopic analyses were performed on pristine barite crystals and on samples which grew in carbonate containing solutions at 50 ºC. The data are listed in Table 3. The Raman spectra of the barite samples were dominated by an intense ν_1 band (symmetric stretching) of SO_4 tetrahedra at 989 cm^{-1} (Fig. 6). The other characteristic bands, ν_2, ν_3 and ν_4 reported in literature (Dimova et al. 2006; Chen et al. 2009; Sánchez-Pastor et al. 2011) were also present (Fig. 6; Table 3). The ν_2 vibration (in-plane bending) generated bands in the 400–500 cm^{-1} region, the ν_4 vibration (out-of-plane bending) generated bands in the 600–700 cm^{-1} region, and the ν_3 vibration (asymmetric stretching) generated bands in the 1080–1200 cm^{-1} region. Figure 6 shows these regions for a pristine barite (barite_pure, grey data) and a crystal that was treated with the growth solution at 50 ºC (barite_c, black data). In both cases, the Raman bands are approximately in the same positions. However, it should be noted that the Raman spectra of crystals are anisotropic. That is, the band positions and relative band intensities may vary slightly depending on the crystal lattice orientation. Figure 7 shows a section of the Raman spectra with the ν_3 band decomposition for the pristine barite

(barite_pure, grey data) and the treated barite (barite_c, black data). Moreover, the Raman spectrum of a natural witherite aggregate has been superimposed. The bands at 1084 cm^{-1}, 1106 cm^{-1}, 1140 cm^{-1} and 1168 cm^{-1} are characteristic of Raman spectra of pure barite and are present in both barite spectra. However, the Raman spectrum of the treated barite shows an additional band at 1059 cm^{-1}. This band was exclusively observed at barite samples which grew in carbonate containing solution and corresponds to the ν_1 internal mode (symmetric stretching) of witherite. Therefore, the band is conclusive for the presence of carbonate groups incorporated within the barite lattice.

On the basis of this finding we speculate that the different effects of carbonate are not only caused by (temporarily) chemisorbed complexes but also by incorporation of carbonate into the barite structure. This two-fold mechanism gives rise to the different growth behavior of islands growing on the pristine barite surface on the one hand and on a barite surface with incorporated carbonate on the other hand. Whereas growth promotion of layers on pristine barite reflects the effects of chemisorption and incorporation, the growth inhibition of subsequent layers is additionally affected by substrate alteration. This alteration is a consequence of carbonate incorporation during growth of the substrate and is the major cause for the observed growth inhibition. Because spreading rates on pristine barite in the presence of carbonate are directly correlated with temperature, we speculate that substrate alteration is a thermally activated process and controls the inverse correlation of temperature and dead zone threshold concentration.

The study is a further example revealing that a single additive can exert opposing effects on crystal growth. Whereas, for example, silicic acids (Pina et al. 2009) or polyaspartate (Elhadj et al. 2006) show an opposing effect on calcite growth depending on additive concentration, the opposing effect of carbonate on barite growth depends on the

specific location of the growth layer. The so called "template effect" (e.g., Astilleros et al. 2010) similarly denotes a location-dependent effect of an additive but does not necessarily imply opposing promotion and inhibition.

ACKNOWLEDGEMENTS

N. Sánchez-Pastor gratefully acknowledges a research fellowship from the Alexander von Humboldt Foundation. Financial support through the Spanish Ministry of Science and Innovation (Project CGL2007-65523-C02-01 and CGL2010-20134-C02-01), the Comunidad de Madrid (Project CAM-2009 910148), and the Deutsche Forschungsgemeinschaft is also gratefully acknowledged. The authors wish to thank Lourdes Fernández-Díaz for helpful comments and Alejandro Fernandez-Martinez, Andrew Stack and two anonymous reviewers for valuable remarks.

REFERENCES CITED

Astilleros, J.M., Pina, CM; Fernández-Díaz, L.; Prieto, M. and Putnis A. (2006) Nanoscale phenomena during the growth of solid solutions on calcite {1014} surfaces. Chemical Geology, 225, 322-335.

Astilleros, J.M., Fernández-Díaz, L. and Putnis A. (2010) The role of magnesium in the growth of calcite: An AFM study. Chemical Geology, 271, 52-58.

Blount, C.W. (1977) Barite solubilities and thermodynamics quantities up to 300ºC and 1400 bars. American Mineralogist, 62, 942-957.

Bosbach, D., Hall, D. and Putnis, A. (1998) Mineral precipitation and dissolution in aqueous solution: in-situ microscopic observations on barite (001) with atomic force microscopy. Chemical Geology, 151, 143-160.

Bracco, J.N., Grantham, M.C. and Stack, A.G. (2012) Calcite Growth Rates As a Function of Aqueous Calcium-to-Carbonate Ratio, Saturation Index, and Inhibitor Concentration: Insight into the Mechanism of Reaction and Poisoning by Strontium. Crystal Growth and Design, 12, 3540−3548.

Cabrera, N. and Vermilyea, D.A. (1958) Growth and Perfection of Crystals. In: R.H. Doremos, B.W. Roberts, and D. Turnbull, Eds., Chapman & Hall, London, 1958, p. 393.

Chen, Y-H., Huang, E. and Yu, S-C. (2009) High-pressure Raman study on the $BaSO_4$-$SrSO_4$ series. Solid State Communications, 149, 2050-2052.

Davey, R.J. (1976) Effect of impurity adsorption on kinetics of crystal-growth from solution. Journal of Crystal Growth, 34, 109-119.

Davey, R.J. and Mullin, J.W. (1974a) Growth of (100) faces of ammonium dihydrogen phosphate crystals in presence of ionic species. Journal of Crystal Growth, 26, 45-51.

Davey, R.J. and Mullin, J.W. (1974b) Growth of [101] faces of ammonium dihydrogen phosphate crystals in presence of ionic species. Journal of Crystal Growth, 23, 89-94.

De Yoreo, J.J., Orme, C.A. and Land, T.A. (2001) Using atomic force microscopy to investigate solution crystal growth. Advances in Crystal Growth Research, 361-380.

Dimova, M., Panczer, G. and Gaft, M. (2006) Spectroscopic study of barite from the Kremikovtsi deposit (Bulgaria) with implication for its origin. Annales Géologiques de la Péninsule Balkanique, 67, 101-108.

Dove, P.M. and Hochella Jr., M.F. (1993) Calcite precipitation mechanisms and inhibition byorthophosphate: in situ observations by scanning force microscopy. Geochimica et Cosmochimica Acta, 57, 705–714.

Elhadj, S., Salter, E.A., Wierzbicki, A., De Yoreo, J. J. . HanN and Dove P. M. (2006) Peptide Controls on Calcite Mineralization: Polyaspartate Chain Length Affects Growth Kinetics and Acts as a Stereochemical Switch on Morphology. Crystal Growth and Design, 6, 197-201.

Freij, S.J., Putnis, A. and Astilleros J.M. (2004) Nanoscale observations of the effect of cobalt on calcite growth and dissolution. Journal of Crystal Growth, 267, 288-300.

Hanor, J.S. (1994) Physical and chemical controls on the composition of waters in sedimentary basins. Marine and Petroleum Geology, 11, 31-45.

Hanor, J.S. (2000) Barite-celestite geochemistry and environments of formation. In: Sulfate Minerals - Crystallography, Geochemistry and Environmental Significance. Reviews in Mineralogy, 69, 423-427.

Higgins S.R., Eggleston C.M., Knauss K. G. and Boro C. O. (1998a) A hydrothermal atomic force microscope for imaging in aqueous solution up to 150°C. Review of Scientific Instruments, 69, 2994–2998.

Higgins, S.R., Jordan, G., Eggleston, C.M. and Knauss, K.G. (1998b) Dissolution kinetics of the barium sulphate (001) surface by hydrothermal atomic force microscopy. Langmuir, 14, 4967-4971.

Higgins, S.R., Bosbach, D., Eggleston, C.M. and Knauss, K.G. (2000) Kink dynamics and step growth on barium sulfate (001): A hydrothermal scanning probe microscopy study. Journal of Physical Chemistry B, 104, 6978-6982.

Higgins, S.R., Jordan, G. and Eggleston, C.M. (2002) Dissolution kinetics of magnesite in acidic aqueous solution: a hydrothermal atomic force microscopy study assessing step kinetics and dissolution flux. Geochimica et Cosmochimica Acta, 66, 3201-3210.

Hartman, P. and Strom, C.S. (1989) Structural morphology of crystals with the barite ($BaSO_4$) structure - a revision and extension. Journal of Crystal Growth, 97, 502-512.

Jordan, G., Pokrovsky, O.S., Guichet, X. and Schmahl, W.W. (2007) Organic and inorganic ligand effects on magnesite dissolution at 100ºC and pH=5 to 10. Chemical Geology, 242, 484-496.

Jordan, G. and Astilleros, J.M. (2006) In situ HAFM study of the thermal dehydration on gypsum (010) surfaces. American Mineralogist, 91, 619-627.

Kubota, N. (2001) Effect of impurities on the growth kinetics of crystals. Crystal Research and Technology, 36, 749-769.

Kubota, N. and Mullin, J.W. (1995) A kinetic model for crystal-growth from aqueous-solution in the presence of impurity. Journal of Crystal Growth, 152, 203-208.

Kubota, N., Fujisawa, Y., Yokota, M. and Mullin, J.W. (1999) Pseudo-solubilities of potassium sulfate in water in the presence of crystal-growth and -dissolution suppressor iron(III) impurities. Journal of Crystal Growth, 197, 388-392.

Land, T.A., Martin, T.L., Potapenko, S., Palmore, G.T. and De Yoreo, J.J. (1999) Recovery of surfaces from impurity poisoning during crystal growth. Nature, 399, 442-445.

Parkhurst, D.L. and Appelo, C.A.J. (2000) User's guide to PHREEQC (version 2): A computer program for speciation, batch-reaction, one-dimensional transport, and inverse geochemical calculations 312 p. US Geological Survey. Water-Resources Investigations Report, 99-4259.

Pina, C.M., Bosbach, D., Prieto, M. and Putnis A. (1998) Microtopography of the barite (0 0 1) face during growth: AFM observations and PBC theory. Journal of Crystal Growth 187, 119-125.

Pina, C.M., Merkel, C. and Jordan, G. (2009) On the bimodal effects of silicic acids on calcite growth. Crystal Growth and Design, 9, 4084-4090.

Rauls, M., Bartosch, K., Kind, M., Kuch, S., Lacmann, R. and Mersmann, A. (2000) The

influence of impurities on crystallization kinetics - a case study on ammonium sulfate. Journal of Crystal Growth 2000, 213, 116-128.

Reyhani, M.M., Oliveira, A., Parkinson, G.M., Jones, F., Rohl, A.L and Ogden, M.I. (2002) In situ characterisation of calcite growth and inhibition using atomic force microscopy. International Journal of Modern Physics B, 16, 25-33.

Risthaus, P., Bosbach, D., Becker, U. And Putnis, A. (2001) Barite scale formation and dissolution at high ionic strength studied with atomic force microscopy. Colloids and Surfaces A-Physicochemical And Engineering Aspects, 191, 201-214.

Sánchez-Pastor, N., Pina, C.M., Fernández-Diaz, L. and Astilleros, J.M. (2006) The effect of CO_3^{2-} on the growth of barite {001} and {210} surfaces: An AFM study. Surface Science, 600, 1369-1381.

Sanchez-Pastor, N., Pina, C.M. and Fernandez-Diaz, L. (2007) A combined in situ AFM and SEM study of the interaction between celestite (001) surfaces and carbonate-bearing aqueous solutions. Surface Science, 601, 2973-2982.

Sánchez-Pastor, N., Aldushin, K., Jordan, G. and Schmahl. W.W. (2010) K^+-Na^+ exchange in phlogopite on the scale of a single layer. Geochimica et Cosmochimica Acta, 74, 1954-1962.

Sánchez-Pastor, N., Gigler, A.M., Jordan, G., Schmahl. W.W. and Fernández-Diaz, L. (2011) Raman Study of Synthetic Witherite-Strontianite Solid Solutions. Spectroscopy Letters, 44, 7500-504.

412 Sangwal, K. (1993) Effect of impurities on the processes of crystal-growth. Journal of Crystal
413 Growth, 128, 1236-1244.
414
415 Sangwal, K. and Owazarek, I. (1993) On the formation of etch grooves at impurity striations
416 and growth sector boundaries in crystals grown from solutions. Journal of Crystal Growth,
417 129, 640-652.
418
419 Stack, A.G., Raiteri, P. and Gale, J.D. (2012) Accurate Rates of the Complex Mechanisms for
420 Growth and Dissolution of Minerals Using a Combination of Rare-Event Theories. Journal of
421 the American Chemical Society, 134, 11-14.
422
423 Sunagawa, I. (1987) Morphology of minerals. In Morphology of Crystals, Part B, ed. by I.
424 Sunagawa, Terra Sci. Pub., Tokyo/ D. Reidel, Dordrecht.
425
426 Sunagawa, I. (1993) In-situ investigation on growth and dissolution of crystals in aqueous-
427 solution. Aquatic Sciences, 55, 347-357.
428
429 van Enckevort, W.J.P., van der Berg, A., Kreuwel, K.B.G., Derksen, A.J. and Couto, M.S.
430 (1996) Impurity blocking of growth steps: Experiments and theory. Journal of Crystal
431 Growth, 166, 156-161.
432
433 Wojdyr, M. (2010) Fityk: A general-purpose peak fitting program, Journal of Applied
434 Crystallography, 43, 1126-1128.
435
436 Kuwahara, Y. (2011) In situ Atomic Force Microscopy study of dissolution of the barite (001)
437 surface in water at 30ºC. Geochimica et Cosmochimica Acta, 75, 41-51.

438 **List of Figure Captions**

439

440 **Figure 1.** AFM images of two-dimensional islands growing on a barite (001) surface at Ω_{barite}
441 = 12, and T = 25°C. (a) Spreading rates of the islands were measured along the [100]
442 directions. (b) Height image showing islands rotated by 180° which were nucleating in the
443 next adjacent monolayer.

444

445 **Figure 2.** Plot of the spreading rates of two-dimensional islands along the [100] direction in
446 pure solutions against 1/T. The linear fit yields an apparent activation energy *Ea* of 38 ± 1
447 kJ/mol. ($R^2 = 0.9979$).

448

449 **Figure 3.** Growth sequence of the barite (001) surface (T = 50°C) in the absence and in the
450 presence of carbonate (*Tc* = 0.06 mM). (a) In the absence of carbonate. (b) The surface is in
451 contact with the carbonate containing solution. (c) The islands on the pristine barite substrate
452 coalesce and complete a monolayer. (d) On the areas that were previously grown in the
453 absence of carbonate, the formation of a new generation of irregular-shape islands can be
454 observed (islands indicated with arrows). (e) When the islands corresponding to the second
455 layer reached a substrate area which grew from a carbonate containing solution, their
456 spreading rate decreased and the shape of the islands changes to elliptical. (f) Carbonate
457 increased the stability of the steps parallel to the [110] direction.

458

459 **Figure 4.** Spreading rates along [100] of two-dimensional islands growing on areas
460 previously grown in the presence of carbonate versus the total carbonate concentration in the
461 aqueous solution. Squares, circles and triangles correspond to 25 °C, 40 °C and 50 °C,
462 respectively.

463

464 **Figure 5.** Plot of the logarithm of the CO_3^{2-}/SO_4^{2-}-ratios at half spreading rate against the
465 reciprocal absolute temperature. The linear fit yields a free energy of carbonate incorporation
466 of $\Delta G = -40 \pm 3$ kJ/mol.
467
468 **Figure 6.** Raman spectra of pristine barite (barite_pure) and barite crystals which grew in
469 carbonate containing solutions (barite_c) showing the dominant Raman band due to the
470 symmetric stretching (ν_1 vibration) of SO_4 located at ~989 cm^{-1}. The ν_2 vibration (in-plane
471 bending) generates bands in the 400 – 500 cm^{-1} region, the ν_4 vibration (out-of-plane
472 bending) generates bands in the 600 – 700 cm^{-1} region, and the ν_3 vibration (asymmetric
473 stretching) generates bands in the 1100 – 1200 cm^{-1} region. Moreover, the characteristic
474 Raman bands due to the external vibration modes are located in the 50 – 250 cm^{-1} region.
475
476 **Figure 7.** Raman spectra of the ν_3 vibration region of the S-O showing the characteristic
477 bands. In the spectrum of barite crystals which grew in carbonate containing solutions
478 (barite_c), an additional band at ~1059 cm^{-1} can be observed. This band corresponds to the
479 symmetric stretching (ν_1 vibration) of CO_3.
480

481 **Tables**

482

483 **Table 1.** Experimental parameters and spreading rates *R* of two-dimensional islands in pure
484 solutions and in solutions containing the minimum amount of carbonate resulting in complete
485 growth inhibition (marked with an asterisk).

486

Temp.	Educts			Carbonate speciation		Ω_{barite}	$\Omega_{witherite}$	pH	R
(°C)	$BaCl_2$ (10^{-5} M)	Na_2SO_4 (10^{-5} M)	Na_2CO_3 (10^{-5} M)	$a(CO_3^{2-})$ (10^{-5} M)	$a(HCO_3^-)$ (10^{-5} M)				(nm/s)
25	4	4	0	~ 0	0.21	12.5	$6.3x10^{-7}$	5.6	0.54 ± 0.01
25*	4	4	20	6.6	11.9	11.5	0.2	10	0
40	5.1	5.1	0	~ 0	0.23	12.5	$1x10^{-6}$	5.6	1.3 ± 0.1
40*	5.1	5.1	10	1.4	8.1	11.9	0.12	9.4	0
50	5.7	5.7	0	~ 0	0.23	12.3	$1.3x10^{-6}$	5.6	1.9 ± 0.1
50*	5.7	5.7	7	0.49	6.2	12.0	0.09	9.1	0
60	6.3	6.3	0	~ 0	0.23	12.5	$1.8x10^{-6}$	5.6	2.8 ± 0.2
70	6.7	6.7	0	~ 0	0.22	12.5	$2.4x10^{-6}$	5.6	4.2 ± 0.3

487

488

489

Table 2. Speciation of solutions used in AFM and Raman (marked with an asterisk) experiments. *Tc*: total carbonate (M); *a*(CO_3^{2-}), *a*(HCO_3^-): species activity; *R1st* (data from Sánchez-Pastor 2006) and *R2nd*: spreading rate of first and second and higher layer islands (nm/s), respectively

		25 ºC				40 ºC				50 ºC			
Tc (10^{-5} M)	**a(CO_3^{2-}) (10^{-5} M)**	**a(HCO_3^-) (10^{-5} M)**	**pH**	**R1st (nm/s)**	**R2nd (nm/s)**	**a(CO_3^{2-}) (10^{-5} M)**	**a(HCO_3^-) (10^{-5} M)**	**pH**	**R2nd (nm/s)**	**a(CO_3^{2-}) (10^{-5} M)**	**a(HCO_3^-) (10^{-5} M)**	**pH**	**R2nd (nm/s)**
0	0	0	5.6	0.54 ± 0.01	0.54 ± 0.01	0	0	5.6	1.3 ± 0.1	0	0	5,6	1.9 ± 0.1
1	0.04	0.93	7,2	0.54 ± 0.01	0.54 ± 0.01	0.01	0.95	7.1	1.3 ± 0.05	0.01	0.95	7	1.9 ± 0.1
2	0.15	1.7	8.8	0.54 ± 0.02	0.54 ± 0.01	0.07	1.8	8.4	1.28 ± 0.08	0.04	1.8	8.2	1.6 ± 0.05
3	0.31	2.5	9.2	0.54 ± 0.01	0.53 ± 0.02	0.15	2.7	8.8	1.24 ± 0.1	0.10*	2.8*	8.5	
4	0.52	3.3	9.4	0.54 ± 0.02	0.53 ± 0.01	0.27	3.5	8.9	1.02 ± 0.03				
5	0.77	4	9.5	0.54 ± 0.02	0.48 ± 0.02	0.41	4.4	9	0.8 ± 0.04				
6	1	4.7	9.5	0.52 ± 0.03	0.43 ± 0.03	0.57	5.2	9.2	0.64 ± 0.01	0.33	5.1	8.9	0.5 ± 0.03
7	1.3	5.3	9.6	0.53 ± 0.02	0.4 ± 0.01					0.49	6.2	9.1	0
8	1.6	5.9	9.7	0.55 ± 0.01	0.38 ± 0.02	0.95	6.7	9.3	0.1 ± 0.04	0.63	7	9.1	0
9	2	6.5	9.7	0.56 ± 0.01	0.36 ± 0.04	1.1	7.4	9.3	0.02 ± 0.01				
10	2.3	7.1	9.8	0.62 ± 0.02	0.31 ± 0.01	1.4	8.1	9.4	0				
11	2.7	7.6	9.8	0.63 ± 0.02	0.27 ± 0.02								
15	4.4	9.7	9.9	0.66 ± 0.02	0.14 ± 0.01	2.7	11	9.5	0				
20	6.6	11.9	10	0.71 ± 0.01	0	4.3	14	9.7	0				
21	7.1	12.3	10		0								
22	7.6	12.7	10		0								

494 **Table 3.** Peak positions (cm^{-1}) of Raman vibrations observed for pristine barite and for barite
495 growing in carbonate containing solution.
496

	MODE ASSIGNMENTS	pristine barite	grown barite
SO_4	**Lattice modes**	57, 72, 90, 127, 149, 190	57, 73, 95, 128, 150, 191
	In-plane bending (ν_2)	459	455
	Out-of-plane bending (ν_4)	618, 647	614, 637
	Symmetric stretching (ν_1)	989	984
	Asymmetric stretching (ν_3)	1084, 1106, 1140, 1168	1085, 1106, 1140, 1168
CO_3	**Symmetric stretching** (ν_1)	/	1059

497
498
499

Figure 1

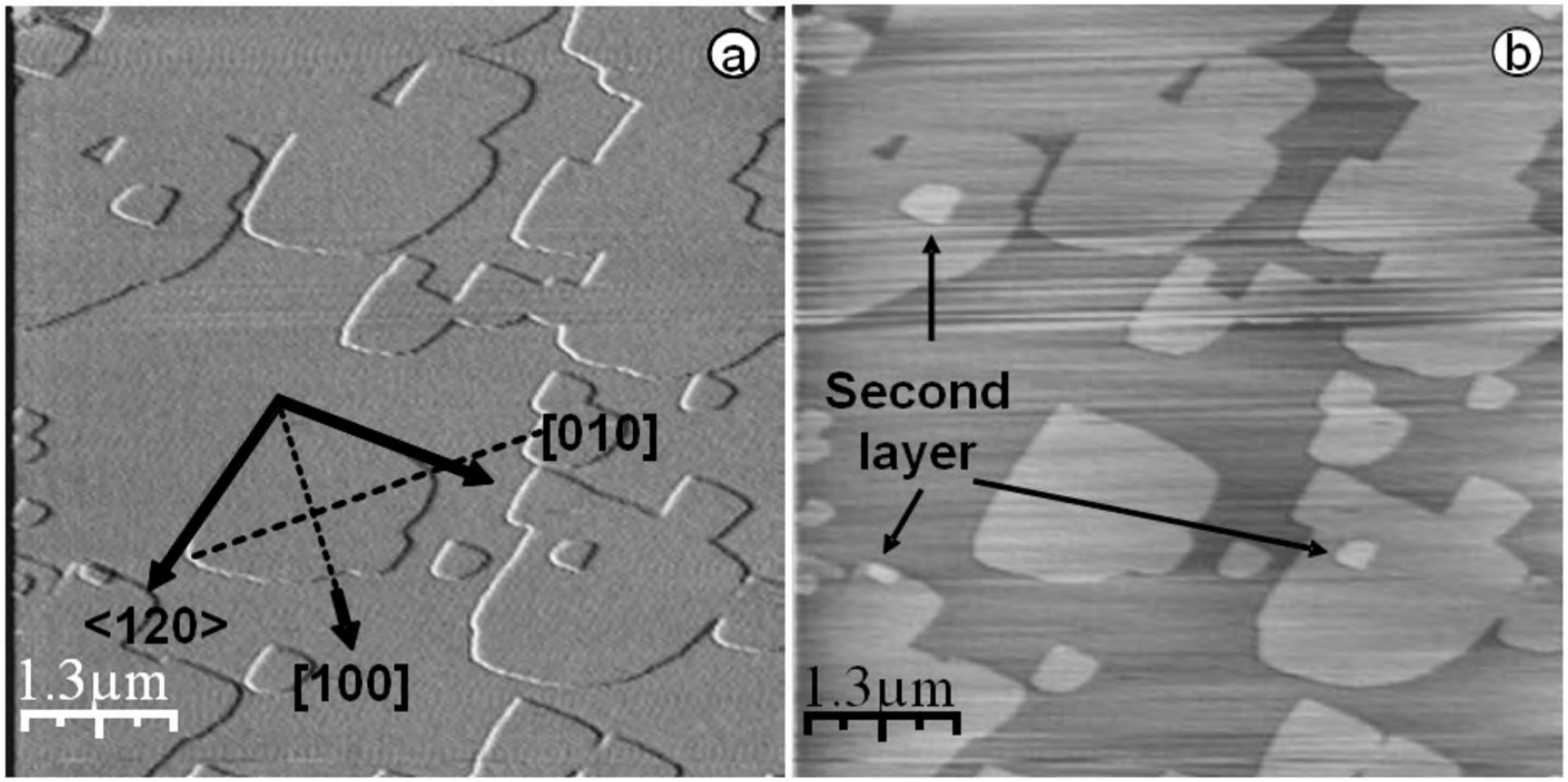

Figure 2

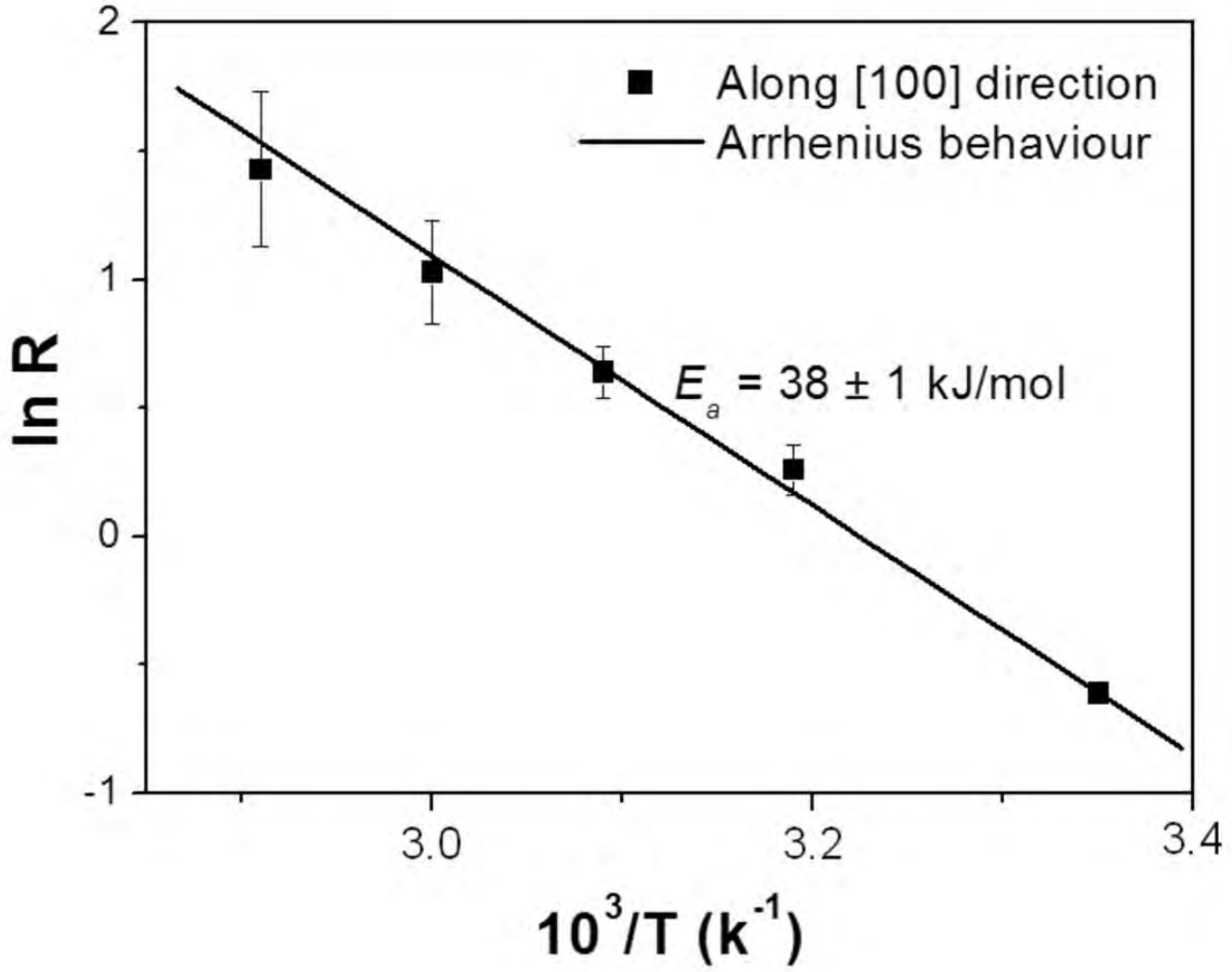
Along [100] direction
Arrhenius behaviour
E_a = 38 ± 1 kJ/mol
ln R
2
1
0
-1
3.0
3.2
3.4
$10^3/T\ (k^{-1})$

Figure 3

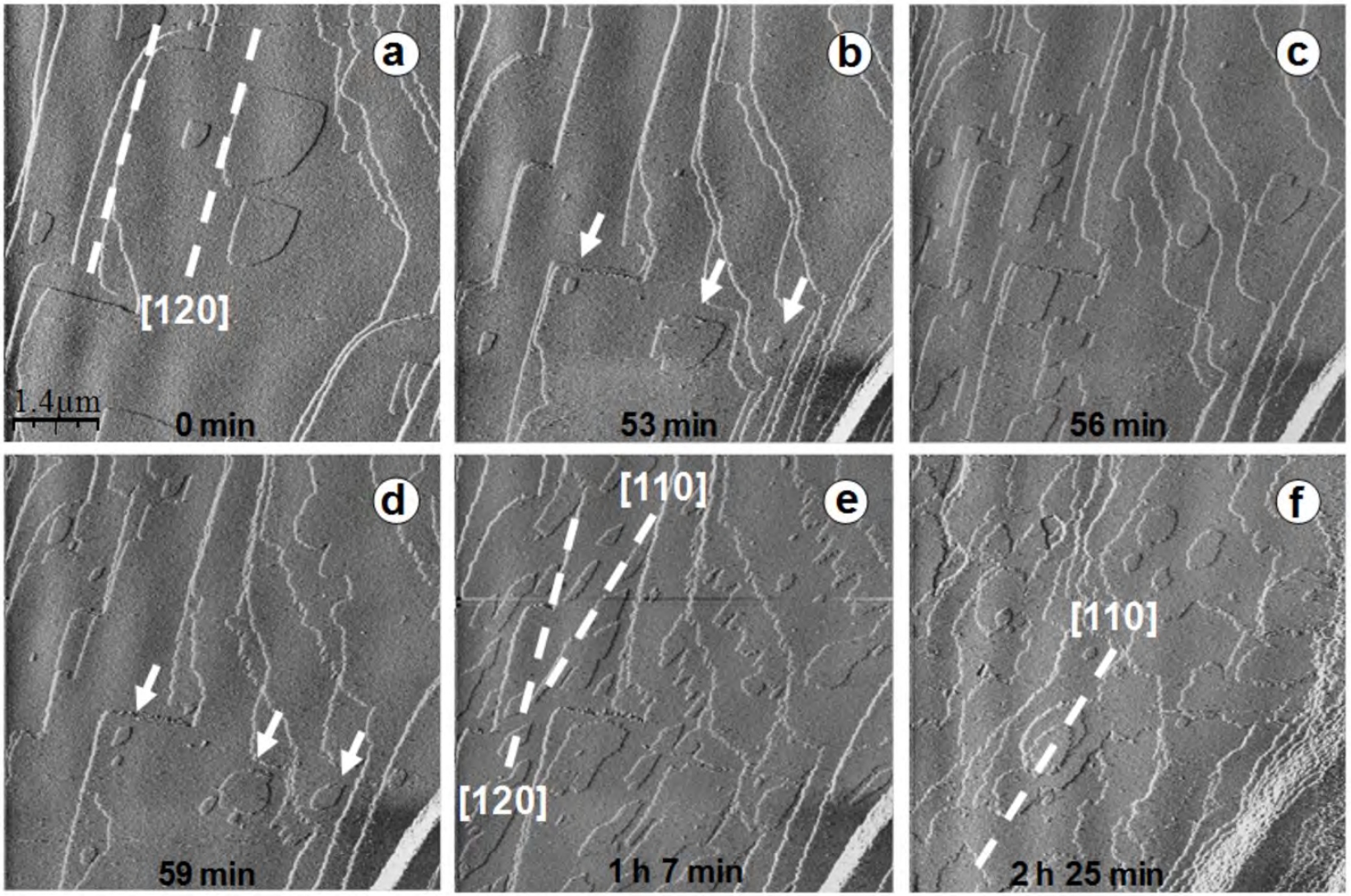
a
[120]
1.4µm
0 min
b
53 min
c
56 min
d
59 min
e
[110]
[120]
1 h 7 min
f
[110]
2 h 25 min

Figure 4

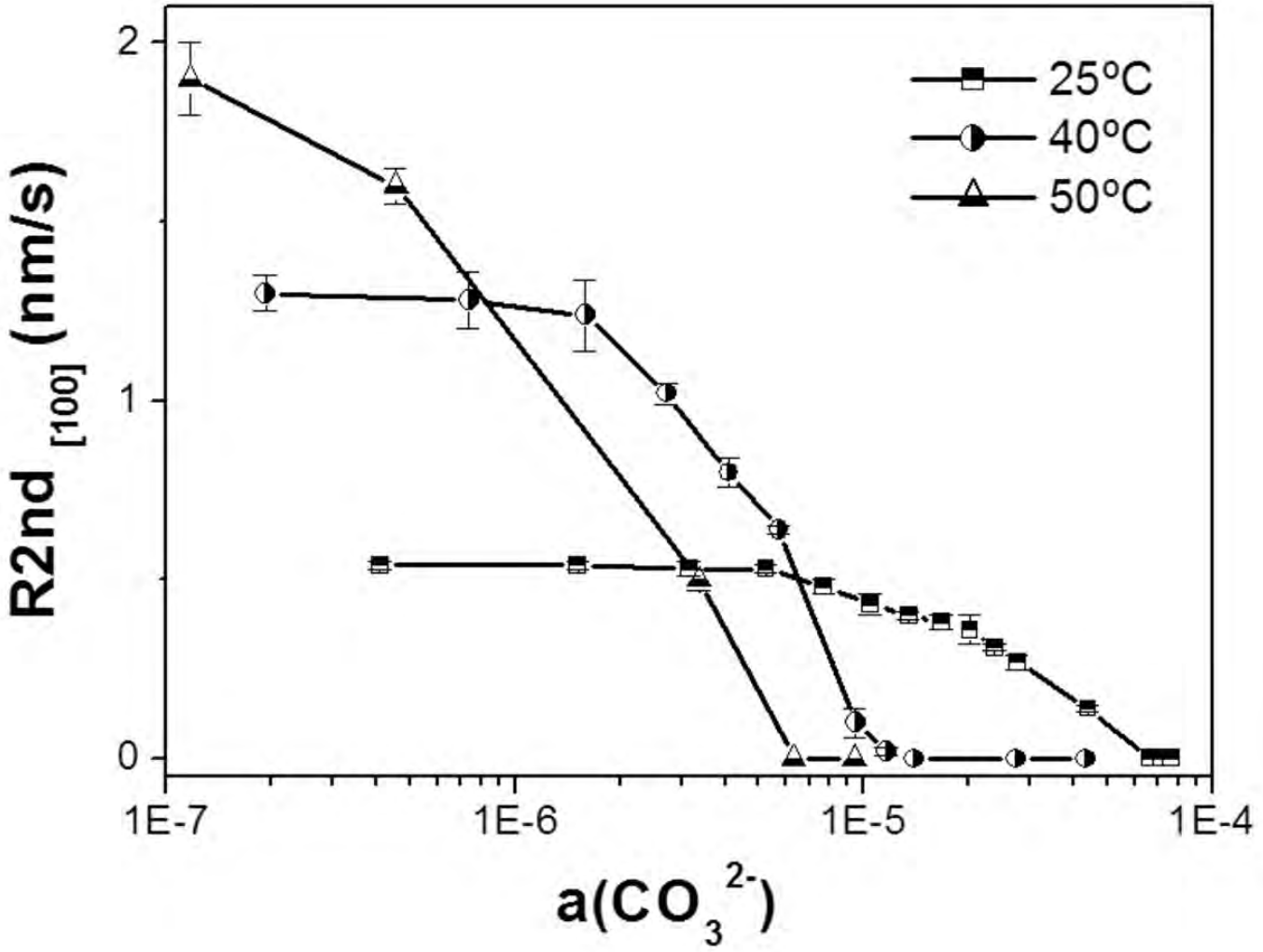

Figure 5

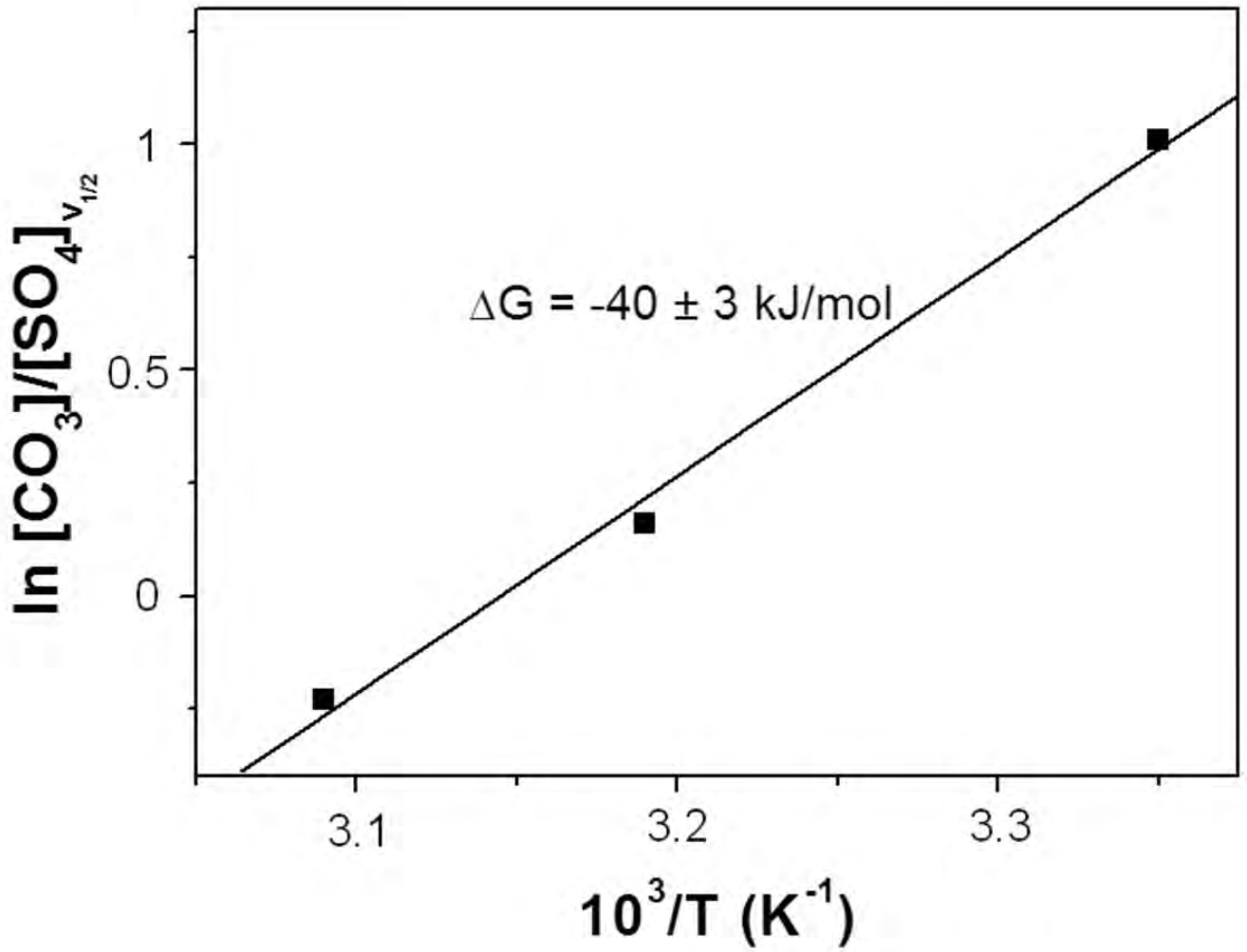

Figure 6

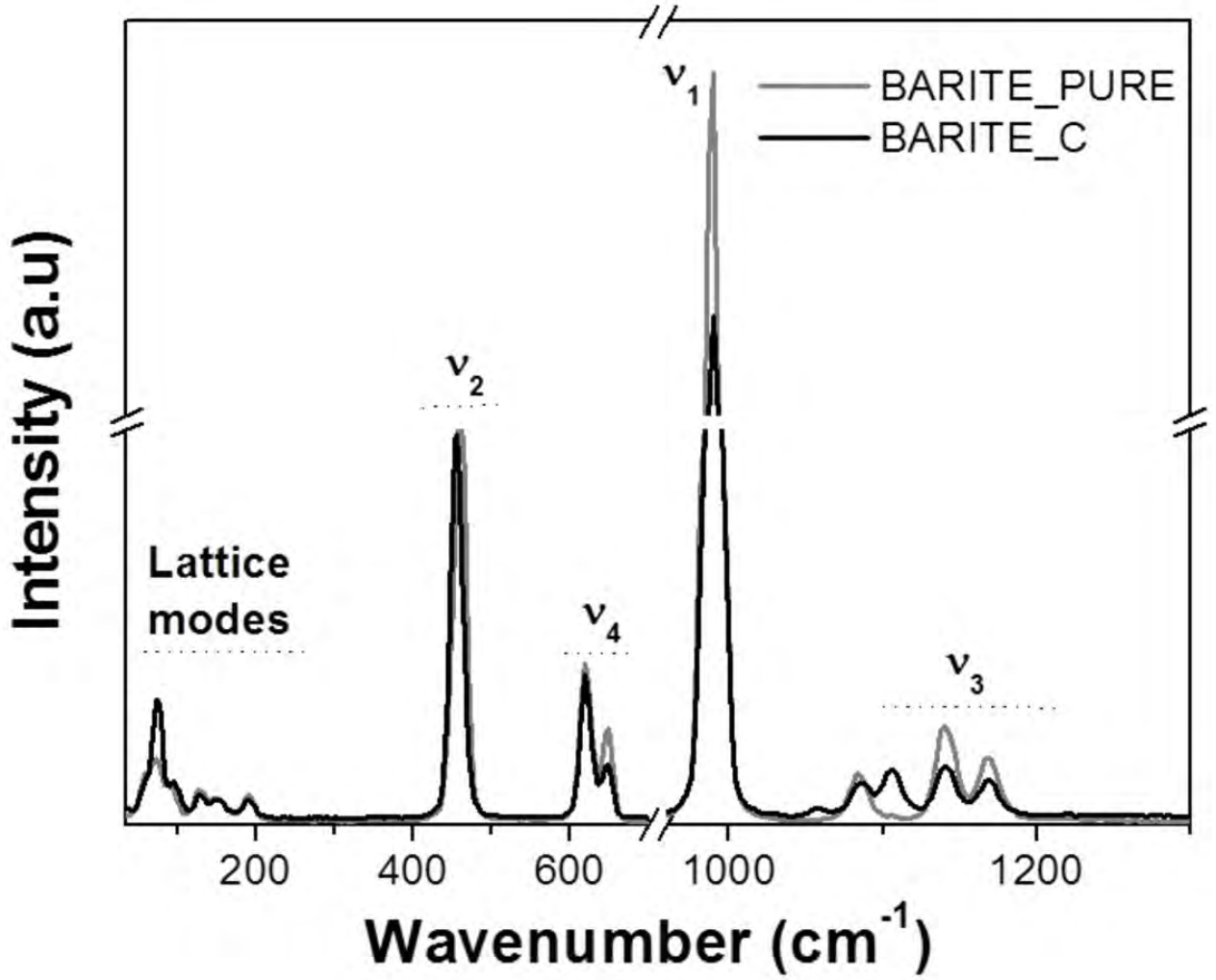
BARITE_PURE
BARITE_C
ν1
ν2
ν4
ν3
Lattice modes
Intensity (a.u)
200
400
600
1000
1200
Wavenumber (cm-1)

This is a preprint, the final version is subject to change, of the American Mineralogist (MSA)
Cite as Authors (Year) Title. American Mineralogist, in press.
(DOI will not work until issue is live.) DOI: http://dx.doi.org/10.2138/am.2013.4420

Figure 7